

# Statistical Properties of a 2D Granular Material Subjected to Cyclic Shear

J. Zhang, T. S. Majmudar, A. Tordesillas<sup>2</sup> and R.P. Behringer<sup>1</sup>

<sup>1</sup>Department of Physics, Duke University, Box 90305, Durham, NC 27708, USA

<sup>2</sup>Department of Mathematics and Statistics, University of Melbourne, Victoria 3010, Australia  
(Dated: February 21, 2024)

This work focuses on the evolution of structure and stress for an experimental system of 2D photoelastic particles that is subjected to multiple cycles of pure shear. Throughout this process, we determine the contact network and the contact forces using particle tracking and photoelastic techniques. These data yield the fabric and stress tensors and the distributions of contact forces in the normal and tangential directions. We then find that there is, to a reasonable approximation, a functional relation between the system pressure,  $P$ , and the mean contact number,  $Z$ . This relationship applies to the shear stress  $\tau$ , except for the strains in the immediate vicinity of the contact network reversal. By contrast, quantities such as  $P$ ,  $\tau$  and  $Z$  are strongly hysteretic functions of the strain,  $\epsilon$ . We find that the distributions of normal and tangential forces, when expressed in terms of the appropriate means, are essentially independent of strain. We close by analyzing a subset of shear data in terms of strong and weak force networks.

## INTRODUCTION

In this work, we describe experiments that probe the microscopic properties of sheared granular materials, with an eye towards understanding the statistical properties and small-scale phenomena which strongly influence larger scale behavior. The application of shear leads to the evolution of a strong force network, as shown in Fig. 1, sometimes referred to as force chains. These mesoscopic structures are filamentary networks that carry forces at or above the mean, and that extend, in the case of shear, over distances of a few to perhaps many tens of grains. During shear, the force network evolves, with force chains strengthening, and then ultimately failing.

The present studies explore the structural evolution of sys-

tem during shear by means of fabric, stress and related tensors. Associated with the evolution of the fabric and stress tensors are a number of complex phenomena, including shear bands, particle rotation, failure and buckling of the force chains, among other effects. We have recently shown the importance of rotation for the failure of force chains, particularly in shear bands [1]. In general, all quantities measured here show fluctuations, and, of course sensitivity to the direction of the shear (forward and reverse). In particular, when the shear direction is switched, the system undergoes structural reconstruction, causing changes in the average contact number, the mean orientation of the contacts, and the stress tensor.

We focus on a path corresponding to pure shear strain, starting from a packing fraction where there is no observable stress. As we strain the system, the detected stresses and mean contact number  $Z$  increase, and the system reaches a jammed state for  $Z$ 's above  $Z' \approx 3$ . As we further deform the system, including reversal of the strain,  $Z$  tends to remain at or above 3 for much of the time. Throughout, multiple shear cycles, the packing fraction  $\phi$  remains at a fixed value,  $\phi = 0.758$ , that is below the observed jamming value for isotropic compression[2]. When the shear strain is reversed, the original force network largely vanishes, and a new strong network forms. This process is strongly hysteretic in the strain, but we find that the stresses can be characterized rather well in terms of the system-averaged contact number,  $Z$ .

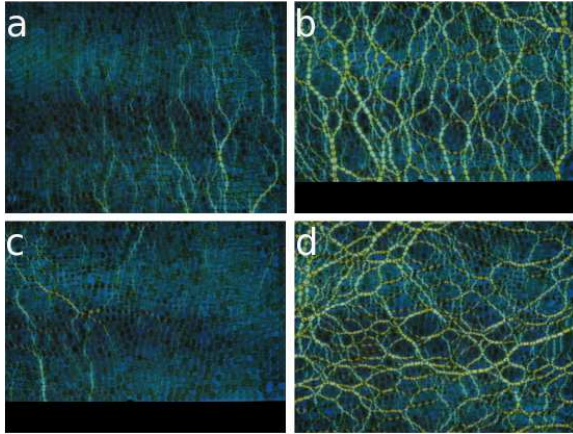


FIG. 1: Sequence of photoelastic images showing the evolution of the force chains as the system is sheared in the forward (images a and b), then the reverse direction (image c and d). These four images are chosen at different steps from the 1st shear cycle, with  $\epsilon = 0.033$ ,  $0.267$ ,  $0.267$ , and  $0.033$ , respectively. The axial strain  $\epsilon$  is defined below. In images b and c, the sidewall of the biax has moved into view, creating dark bands at the bottom of the images.

In the remainder of this work, we first describe basic features of the experimental techniques. We then present results from cyclic pure shear experiments, in which we explore the structural and stress changes within each shear cycle and in particular during shear reversals. We then analyze the force network in terms of strong and weak components.

## EXPERIMENTAL TECHNIQUES

The experiments described here use a ‘biaxial’ apparatus, as depicted in the upper parts of Fig. 2. This device allows us to deform a rectangular sample of particles into any other desired rectangular shape, hence apply pure shear (compression in one direction, but equal dilation in the other), uniaxial compression, isotropic compression, etc. Here, we focus uniquely on shear deformations, which maintain a fixed area for the system.

The studies are carried out effectively in 2D by using disks which are made of photoelastic material. When under stress, and when viewed between crossed polarizers, photoelastic materials exhibit a series of light and dark bands, as in the bottom left image of Fig. 2. These bands encode the detailed stress within each particle, and these stresses are in turn, determined by the forces at contacts on each particle. In the past, this technique has been used in several different studies [3, 4]. What makes our current approach unique is that, for large collections of particles, we solve the inverse problem which starts from the photoelastic image and yields as output, the inter-particle contact forces. More details have been given elsewhere [1, 5, 6]. The particles are also typically marked with a small bar, which allows us to track the rotation and displacement of individual particles. In our current tracking approach, the bars are drawn on with fluorescent ink, which is invisible under ordinary light but glows strongly under UV light. In this way, it is possible to have both photoelastic images for force/stress measurement and separate images for tracking rotation and displacement of a given set of particles, without mutual interference. In earlier versions of this approach [7, 8, 9, 10, 11], we used solid black bars drawn on the particles. In this case, we imaged separate sets of particles for determining forces and for tracking motion.

The initial boundaries of the system form a square filled with 1568 bi-disperse photoelastic disks at a packing fraction  $\phi = 0.758$ . There are roughly 80% smaller particles having a diameter of 0.74 cm, and 20% larger particles having a diameter of 0.86 cm. The initial state is prepared as close to isotropic as possible and is stress-free. The system is then subjected to shear by compression along the  $y$ -direction and expansion along the  $x$ -direction, as in Fig. 2 (top-left), keeping the system area constant. Since the area is fixed, the deformation can be simply defined using the strain  $\epsilon$  along the  $x$ -axis with  $\epsilon = (x - x_0)/x_0$ . Here,  $x_0$  is the initial size of the square. Once a maximum deformation  $\epsilon_{max}$  is reached, shear is reversed by compression along the  $x$ -axis and expansion along the  $y$ -axis. After this first shear reversal, the shear continues until the system domain returns to a square, and then deforms in the negative strain direction. Once  $\epsilon$  reaches a minimum  $\epsilon_{min} < 0$ , a second shear reversal is applied, eventually returning the system domain to a square with  $\epsilon = 0$ . This completes one shear cycle. The second shear cycle continues from the final state of the first shear cycle and the same procedure is applied for a total of six shear cycles. Note that the actual val-

TABLE I: A list of  $\epsilon_{max}$  and  $\epsilon_{min}$  for different shear cycles.

Shear cycle	$\epsilon_{max}$	$\epsilon_{min}$
1	0.2867	-0.15
2	0.29	-0.15
3	0.2333	-0.15
4	0.2	-0.15
5	0.1833	-0.1667
6	0.15	N/A

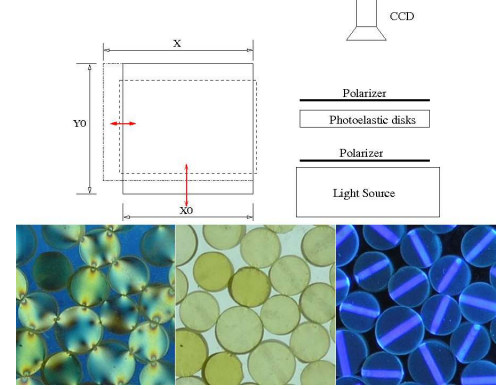


FIG. 2: Top-left: Sketch of top view of the experimental apparatus, a 2D ‘biax’, consisting of pairs of facing boundaries that can be moved precisely under computer control so as to produce desired strains. Particles rest on a smooth slippery sheet of Plexiglas and are confined laterally by the walls of the biax. Strains are applied quasi-statically, in small discrete steps. Top-right: Side view of apparatus. Imaging is carried out by a camera mounted above the biax, and for each step, we obtain three images: one with crossed polarizers (bottom left), one without polarizers (bottom center), and one without polarizers but with UV illumination (bottom right).

ues of  $\epsilon_{max}$  and  $\epsilon_{min}$  are different for each shear cycle and the possible extreme values for these are determined by the spatial limit of the apparatus. A list of  $\epsilon_{min}$  and  $\epsilon_{max}$  are summarized in Table I. The whole shear process is carried out in small incremental quasi-static steps. From one step to the next,  $\epsilon$  increases or decreases by a small amount  $\delta\epsilon = 3.3 \times 10^{-3}$ , depending on the shear direction. After each step, the motion is paused and images are acquired. The three images in the bottom row Fig. 2 show close-ups of the three different image types. The left-most of these is taken with polarizers in place, the middle is without polarizers and with ordinary light, and the right-most is without polarizers and with UV light.

Before we turn to detailed results we note an experimental issue of importance. During the parts of the cycle where the overall stresses in the system are low, the photoelastic response at some contacts falls below our limit of resolution. Because, as discussed below, the experiments indicate a distribution of normal contact forces of the form

$$P(F_n) = \frac{1}{\Gamma} f(F_n/\Gamma); \quad (1)$$

where  $f$  is to a reasonable approximation, the same function for all mean forces, we can estimate the number of the missed

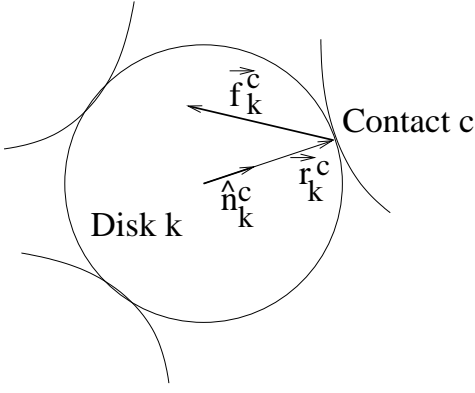


FIG. 3: Sketch illustrating the notation for calculating the fabric, force-moment and stress tensors.

contacts reasonably well. Non-zero contact forces below our experimental resolution also affect our measurements of stress and, in particular,  $P$ . However, the effect on stress components is much lower, since the contact forces appear linearly in the appropriate sums.

We expect that we miss a fraction

$$\int_0^{F_c} P(F_n) dF_n = \int_0^\infty P(F_n) dF_n \quad (2)$$

of contacts, where  $F_c$  is a small known cut-off force, roughly the weight of a particle, below which we cannot detect the photoelastic response. This means that the measured  $Z$ 's are lower than their true values by

$$\int_{F_c}^\infty P(F_n) dF_n = \int_0^\infty P(F_n) dF_n : \quad (3)$$

We also underestimate the pressure by a factor of

$$\int_{F_c}^\infty F_n P(F_n) dF_n = \int_0^\infty F_n P(F_n) dF_n : \quad (4)$$

In this last expression, we assume that all particles have the same radius, which is a reasonably good assumption. In this regard, the correction can be as much as 15% in  $Z$  very near jamming, but then becomes negligible for  $Z$  a bit above 3.0. The correction to  $P$  is much smaller, only 1-2% close to the jamming transition. In order to simplify the correction, we assume that the force distribution is an exponential. This is roughly right, and produces a reasonable correction, given the statistical variability of the data. The results of  $P$  and  $Z$  presented in this paper have been corrected accordingly. We use the same correction factor for shear stresses,  $\tau$ , although in this case, the correction is not a rigorous.

## EXPERIMENTAL RESULTS

We are concerned with the evolution of the force and contact networks. Both are typically strongly anisotropic, and the

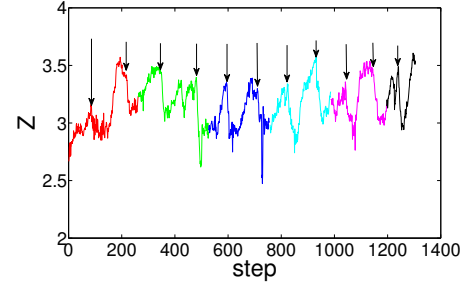


FIG. 4: Evolution of the average contact number  $Z$  vs. step number  $N_s$ . Each shear cycle is colored differently. Arrows indicate the steps where the shear direction is switched.

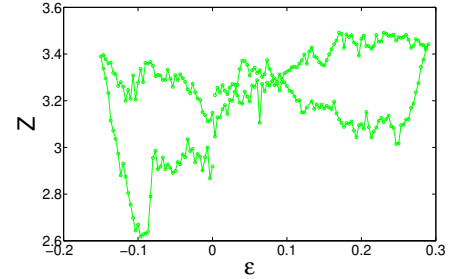


FIG. 5: Mean contact number  $Z$  vs. strain  $\epsilon$  for the second cycle.

direction of the anisotropy switches quickly when the direction of strain is reversed. The force anisotropy is evident in Fig. 1, which shows representative photoelastic images during different phases of a single cycle. The structural changes of the contact network during cyclic shear are also strongly anisotropic. These can be captured by the fabric tensor,  $R_{ij}$ , defined as

$$R_{ij} = \frac{1}{N} \sum_{k=1}^N \sum_{c=1}^{c_k} n_{ik}^c n_{jk}^c : \quad (5)$$

Here, the summation and  $N$  include only non-rattler disks, and as illustrated in Fig. 3,  $c_k$  is the number of contacts on disk  $k$ , and  $n_{ik}^c$  is the  $i$ th component of the unit branch vector pointing from the center of the disk  $k$  to a contact  $c$ . We consider a rattler disk to have less than two detectable contacts. The average contact number  $Z$  is simply the trace of the fabric tensor  $R_{ij}$ . The principal eigendirection of  $R_{ij}$  is also a useful measure of the prevailing orientation of the force network.

Figs. 4 and 5 show how  $Z$  changes in each shear cycle as a function of step number  $N_s$  for all cycles, and as a function of strain  $\epsilon$  for one cycle. In Fig. 4, the individual shear cycles are distinguished using different colors. We will maintain this color scheme throughout to identify the various cycles. Arrows in Fig. 4 indicate the shear reversals.  $Z$  fluctuates between a minimum value of around 2.5 and a maximum value of around 3.5. The first shear cycle, the red curve, begins with a nearly stress-free and isotropic state. The force chains build up steadily. As a consequence,  $Z$  increases as more force chains develop.  $Z$  barely exceeds 3 before the first shear re-

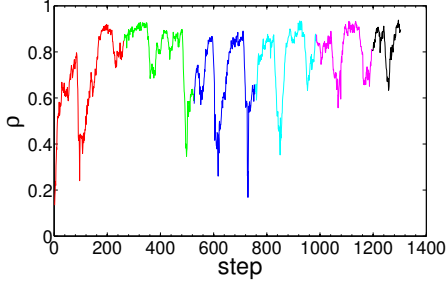


FIG. 6: Evolution of the ratio,  $\rho$ , vs. step number,  $N_s$ .  $\rho$  is defined as the number of non-rattler particles over the total number of particles.

versal. Immediately after the reversal,  $Z$  drops. The relatively rapid decrease of  $Z$  after a switch of the shear direction is common to all shear reversals because the force network/force chains switch direction during this transition. With continued strain after a reversal,  $Z$  again increases as a new strong network, orthogonal to its predecessor, emerges. Note that  $Z = 3$  is the nominal isostatic point for frictional particles in two dimensions. Fig. 4 shows that the system remains mostly in a jammed state after the first cycle, but that it may leave a jammed state briefly after shear reversal. As we show below, shear bands form in response to the shear. Hence, these states are not spatially homogeneous. However, it is the presence of a mechanically rigid but dilated region in the shear bands that allows for jammed states at  $\phi$ 's lower than the isotropic value. We also emphasize that  $Z$  is strongly hysteretic when viewed with respect to strain. To demonstrate this point, we show one shear cycle, the second, as a function of strain in Fig. 5.

At various steps, the fraction,  $\rho$ , of detectable non-rattler particles also fluctuates, as displayed in Fig. 6. This ratio changes from 0.2 up to 0.90. Both Fig. 4 and Fig. 6 show similar trends, although  $\rho$  is noisier at the step where shear is reversed.

We characterize the mean anisotropy of the contact network in terms of  $\vartheta$ , the system-averaged value of the angle between the eigenvector of the maximum eigenvalue of  $R$  and the  $x$  axis. Here, we restrict  $0 < \vartheta < 180^\circ$ . Figure 7 shows that  $\vartheta$  switches quickly, shortly after each strain reversal. That is, after a very small strain,  $\vartheta$  aligns with the compressive direction. In order to see how quickly the angle changes after a shear reversal, we have plotted  $\vartheta$  on a much finer scale. The results are presented in Fig. 8, where the graphs are organized from top to bottom, as a function of step number,  $N_s$ . The typical number of steps required for the readjustment of the orientation varies from  $\Delta N_s \sim 10$ . However, we note that there is often a lag between the strain reversal, and the switch in  $\vartheta$ , which may occur in only a few strain steps.

The stress tensor  $\sigma_{ij}$  and the force moment tensor,  $\hat{\sigma}_{ij}$  provide additional measures of anisotropy, in this case for the forces. We define a local force moment tensor as

$$\hat{\sigma}_{ij} = \sum_{c=1}^{c_k} f_{ik}^c r_{jk}^c : \quad (6)$$

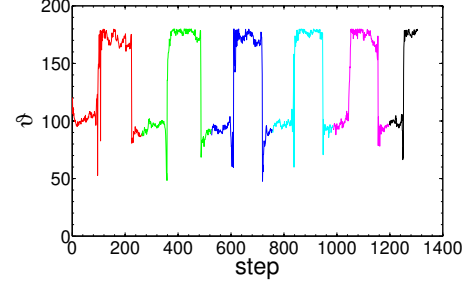


FIG. 7: Fabric orientation angle  $\vartheta$  vs. step number,  $N_s$ .  $\vartheta$  is defined as the absolute angle between the eigenvector of the maximum eigenvalue of the fabric tensor  $R$  and the  $x$  axis. This angle measures the dominant contact orientation

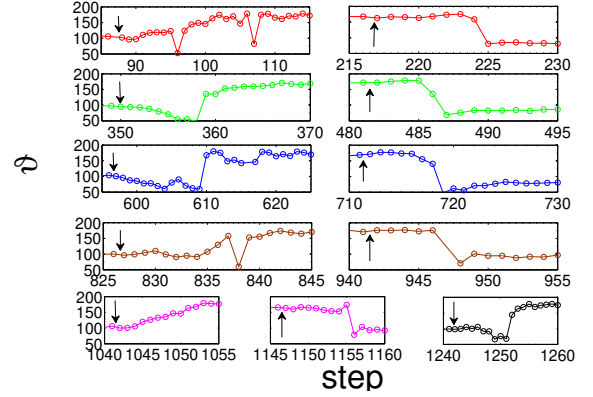


FIG. 8: Fabric orientation angle  $\vartheta$  vs. step number  $N_s$  on a fine scale near shear reversals. Arrows in each graph indicate the beginning of the shear reversals. The readjustment of  $\vartheta$  after a shear reversal takes about 10 to 20 steps.

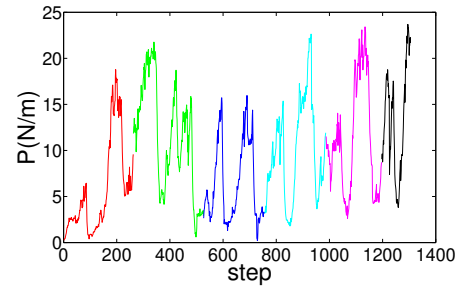


FIG. 9: Pressure  $P$  vs. step number  $N_s$ .

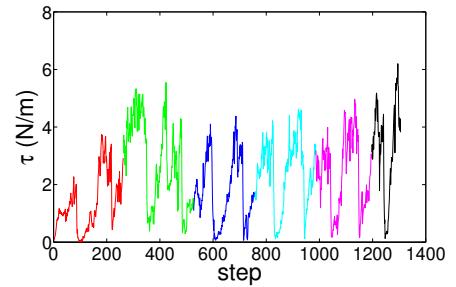


FIG. 10: Shear stress  $\tau$  vs. step number  $N_s$ .



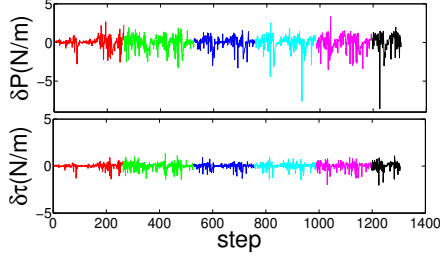


FIG. 11:  $\delta P$  (top) and  $\delta \tau$  (bottom) vs. step number  $N_s$ .  $\delta P$  and  $\delta \tau$  are respective differences between two neighboring steps of  $P$  and  $\tau$  as given in Fig. 9 and Fig. 10.

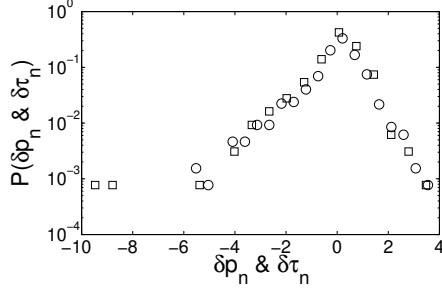


FIG. 12: PDFs of  $\delta p_n$  (circles), and  $\delta \tau_n$  (squares).  $\delta p_n$  and  $\delta \tau_n$  are made dimensionless through normalization by their corresponding standard deviations.

The globally averaged stress tensor is then

$$\sigma_{ij} = \frac{1}{A} \sum_{k=1}^N \hat{\sigma}_{ij} : \quad (7)$$

Here,  $A$  is the system area;  $N$ ,  $c_k$ ,  $i$ ,  $r_{jk}^c$  and  $j$  have the same meaning as in the expression of  $R_{ij}$  (e.g. Fig. 3).  $f_{ik}^c$  is the  $i$ th component of the contact force on particle  $k$  at contact  $c$ . The two eigenvalues of the stress tensor are  $\sigma_1$  and  $\sigma_2$ , where  $\sigma_1 \geq \sigma_2$  by definition. The pressure is then  $P = \frac{1}{2}(\sigma_1 + \sigma_2)$  and the shear stress is  $\tau = \frac{1}{2}(\sigma_2 - \sigma_1)$ .

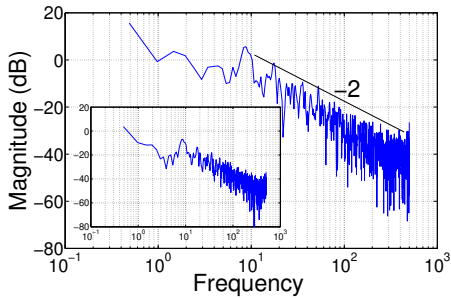


FIG. 13: Power spectra, on log-log scales, for  $\delta p_n$ , (inset) and  $\delta \tau_n$  computed from the data given in Fig. 9 Fig. 10 vs. frequency corresponding to inverse step number, where a frequency of  $1\text{ Hz}$  corresponds to a  $1=1000$  steps. The solid line is a guide to the eye, and corresponds to a power law with an exponent of  $-2$ .

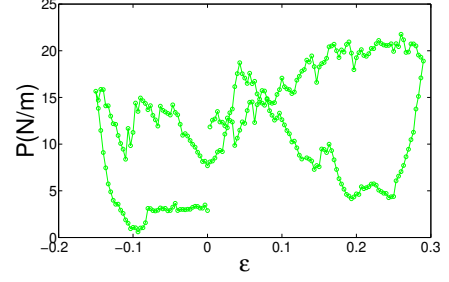


FIG. 14: Pressure,  $P$  vs. strain,  $\epsilon$ , for the second cycle, showing strong hysteresis.

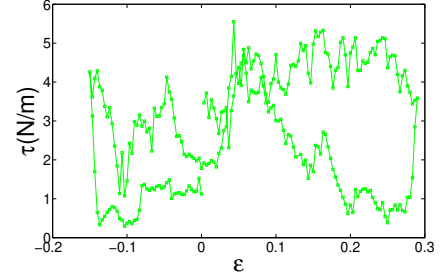


FIG. 15: Shear stress  $\tau$  vs. strain,  $\epsilon$  for the second cycle.

Figure 9 and Fig. 10 show the evolution of the pressure and the shear stress versus step number,  $N_s$ , and Figs. 14 and 15 show  $P$  and  $\tau$  over the second cycle vs. strain. Both  $P$  and  $\tau$  vary significantly with strain, but unlike  $\vartheta$ , both quantities evolve steadily, modulo some significant fluctuations, up to the maximum of a given cycle. The fluctuations evident in the stress evolution are due to failure events, which are associated with a continual collapse of old and formation of new force chains. To show the scale of the fluctuations more clearly, we present in Fig. 11, the changes  $\delta P$  and  $\delta \tau$  in  $P$  and  $\tau$ , respectively, between successive steps. The curves exhibit random spikes in the positive and negative directions. It is perhaps worth emphasizing that the fluctuations, even for these system-averaged stress differences, can be large relative to the locally averaged step sizes, which cannot be distinguished from zero on these plots. Figure 12 shows the probability distribution functions (PDF's) of  $\delta P$  and  $\delta \tau$ , after normalizing by their respective standard deviations. The two PDF's for  $\delta p_n$  and  $\delta \tau_n$  are virtually indistinguishable, and decay exponentially for positive and negative values, with a somewhat more rapid decay for positive values. Sharp drops of  $P$  and  $\tau$  occur at steps where the shear is reversed. Each drop is associated with the release of stored mechanical energy. Interesting issues include the nature of the energy dissipated, and the relation to the evolution of the force network ([1, 12, 13]). For instance, recently, we have found that buckling of the force chains [1] is an important mechanism leading to the loss of energy in shear. We will address these questions in future work.

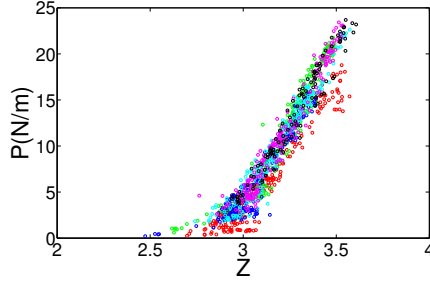


FIG. 16: Pressure,  $P$ , vs. average contact number,  $Z$ . Different colors correspond to data from different shear cycles. Data points from the first shear cycle, shown in red, deviate slightly from other shear cycles.

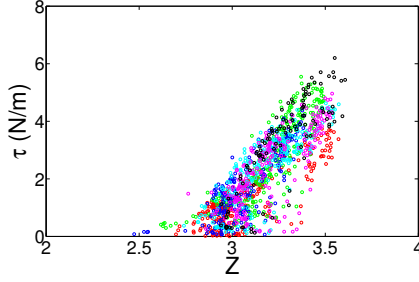


FIG. 17: Shear stress,  $\tau$  vs. average contact number,  $Z$ .

To further examine the fluctuations of  $P$  and  $\tau$ , we analyzed their power spectra from the curves in Figs. 9 and 10. Here, we use step number,  $N_s$ , as a time-like variable, and  $(N_s=1000)^{-1}$  as a frequency-like variable. The spectra vs. frequency variable, shown in Fig. 13 are similar for  $P$  and  $\tau$ , and are typically broad-band. They suggest a power law decay with an exponent close to  $-2$  for both  $P$  and  $\tau$ . Similar behavior for the high-frequency part of the spectrum has been reported in previous experiments on continuously sheared 3D granular systems [14].

It is clear from Figs. 5, 14, and 15 that the stresses and  $Z$  are hysteretic in the strain, i.e., that the strain does not provide a

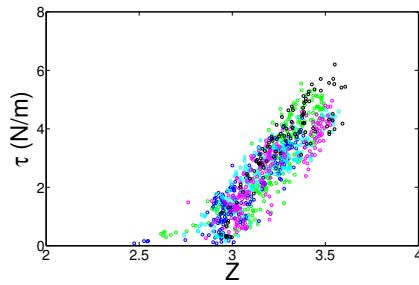


FIG. 18: Shear stress,  $\tau$  vs. average contact number,  $Z$  after removal of data points from the first shear cycle and data points where the strong network direction, as measured by  $\vartheta$ , is switching directions, as in Fig. 8.

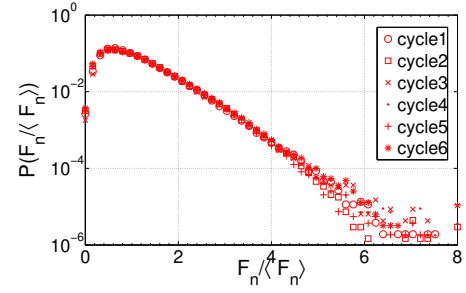


FIG. 19: Data for the distribution of normal forces,  $F_n$ , expressed as  $F_n = \langle F_n \rangle$  of all six shear cycles. We show data from all strain steps collectively for each cycle. Here, data for  $F_n = \langle F_n \rangle$  are normalized by  $\langle F_n \rangle$  for the given step.

unique characterization of a state. It is then interesting to ask whether there is some other quantity that better characterizes the nature of a given state, and in particular whether there is a relation among  $Z$  and  $P$  and  $\tau$ . For jamming of spherical (circular in 2D) particles under isotropic stress conditions, the key control parameter is the density/packing fraction. Then, both  $Z$  and  $P$  are functions of  $\phi$ , and consequently,  $P$  is a function of  $Z$ . Here, however, the packing fraction is constant. Yet, starting from an unjammed state, we arrive at a state which is jammed when we apply sufficient shear. In order to address what might control jamming in this case, we note that Figs. 5, 14, and 15 show similar shapes. Drawing on the isotropic stress case, we ask whether a relation exists between  $Z$  and the stresses.

Indeed, Fig. 16 shows that data for  $P$  vs.  $Z$  fall on a nearly common curve. In a similar fashion,  $\tau$  vs.  $Z$  falls on a nearly common curve. For  $\tau$  vs.  $Z$ , the relative scatter is higher. However, there is a systematic part of the  $\tau$  vs.  $Z$  data that fall below the weight of the curve. These data correspond to relatively small ranges of strain following a reversal. As  $\vartheta$  switches direction, the system passes through a more nearly isotropic state. In addition,  $\tau$  vs.  $Z$  data from the first cycle start from an isotropic state for which  $\tau = 0$ . For the first part of that cycle, the system retains some memory of its initial state. If the data from the first cycle and immediately after reversals are removed, the results for  $\tau$  vs.  $Z$  yield a collapse that is comparable to that for  $P$  vs.  $Z$  as seen in Fig. 18. Although  $P$  and  $Z$  do collapse, the spread of the data points around the curve is still quite big. This spread reflects statistical fluctuations, which as shown above, can be large even for the system-averaged  $P$  and  $\tau$ . An interesting observation is that except for the switching regimes, in the mean, the ratio  $\tau/P = \text{constant}$ . In this case, the relation follows because  $\tau$  and  $P$  are separately (essentially) linear functions of  $Z$  and both vanish at the common value  $Z' \approx 3$  where the system first jams.

Additional statistical measures include the distribution of contact forces, including the normal force distribution given in Fig. 19 and the tangential force distribution given in Fig. 20. In these figures, we have organized the data by cycle number,

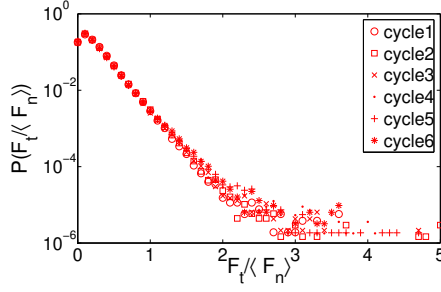


FIG. 20: Data for the distribution of normalized tangential forces,  $F_t = \langle F_n \rangle$  of all six shear cycles. As for the distribution of normal forces, the statistics are combined for all steps within each cycle, where the normalization,  $\langle F_n \rangle$  is made for each step.

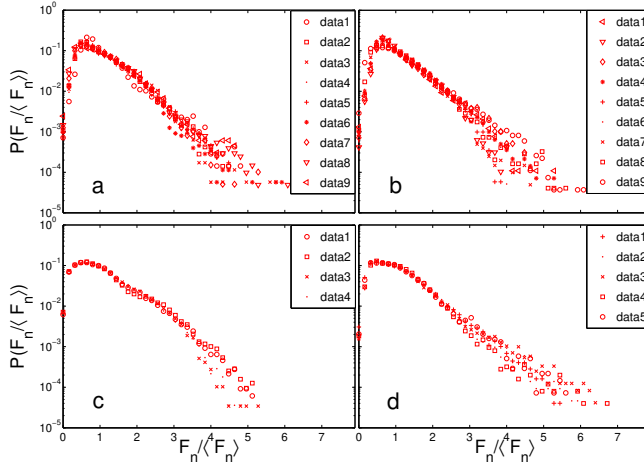


FIG. 21: Data for the distribution of normal forces,  $F_n$ , expressed as  $F_n = \langle F_n \rangle$  in the first shear cycle. (a) distribution  $P(F_n = \langle F_n \rangle)$  for forward shear,  $\epsilon > 0$ . (b)  $P(F_n = \langle F_n \rangle)$  for reverse shear when  $\epsilon = 0$ . (c)  $P(F_n = \langle F_n \rangle)$  for reverse shear when  $\epsilon < 0$ . (d)  $P(F_n = \langle F_n \rangle)$  for forward shear when  $\epsilon = 0$ . To improve statistics, each data point on the graph includes a set of  $F_n = \langle F_n \rangle$  from 10 neighboring steps in most cases. A summary of each data point and its corresponding steps and strains can be found in Table II.

and we have combined data for different steps within a cycle. Here, we normalized the data for  $F_n$  or  $F_t$  for each step by the the mean normal force  $\langle F_n \rangle$  at that step. To justify that this is legitimate, we plot the distributions of  $F_n = \langle F_n \rangle$  and  $F_t = \langle F_n \rangle$  for different strain steps within the first shear cycle in Figs. 21 and 22. Several neighboring steps, ten for most data points and three to five for data near a reversal, are combined for each data point on the plots. The details are summarized in Table II. Some strain steps may have a longer tail than others but their general shapes are more or less similar, and in particular, there is no systematic difference between distributions for different steps. As always, the tails show bigger scatter due to limited statistics.

The distributions of normal forces show a common form consisting of a nearly exponential fall-off at large  $F_n = \langle F_n \rangle$  and a peak at low  $F_n = \langle F_n \rangle$ . At the extreme tails, the distributions

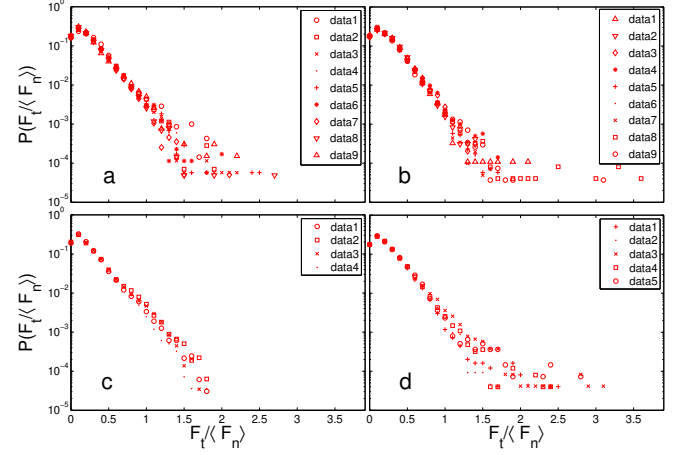


FIG. 22: Data for the distribution of tangential forces,  $F_t$ , expressed as  $F_t = \langle F_n \rangle$  in the first shear cycle. (a) distribution  $P(F_t = \langle F_n \rangle)$  of the forward shear when the strain  $\epsilon > 0$ . (b)  $P(F_t = \langle F_n \rangle)$  of the inverse shear when  $\epsilon = 0$ . (c)  $P(F_t = \langle F_n \rangle)$  of the inverse shear when  $\epsilon < 0$ . (d)  $P(F_t = \langle F_n \rangle)$  of the forward shear when  $\epsilon = 0$ . To improve statistics, each data point on the graph includes a set of  $F_t = \langle F_n \rangle$  from 10 neighboring steps. See details in Table II.

differ somewhat, but this is to be expected because the statistics are limited there.  $P(F_t = \langle F_n \rangle)$  also shows an exponential decay, except that the tangential force distribution, as a function of  $P(F_t = \langle F_n \rangle)$ , decays faster than that for the normal forces. However, this is simply due to the choice of normalization. That is, if the tangential forces were normalized by  $\langle F_t \rangle$ , then the rate of exponential fall-off would be comparable to that for the normal force distributions. For small  $F_n = \langle F_n \rangle$  and  $F_t = \langle F_n \rangle$ , both distributions fall below exponentials. Although some of the fall-off is due to the experimental lower limit of force detection, we believe that this is a relatively minor effect. Specifically, the shape of the distribution is not particularly sensitive to the mean force.

## CONNECTION TO SHEAR LOCALIZATION AND FORCE CHAIN EVOLUTION

We next explore possible connections between the hysteresis observed in these experiments and two defining aspects of material behavior under shear: shear banding and stick-slip (e.g. [12, 15]). These two mechanisms are related and are both governed by force chain/force network evolution. Note that we use the term ‘stick-slip’ to signify fluctuations in the macroscopic stress, in particular, that of the stress ratio,  $\tau = P$ . Specifically, stick and slip events are periods where the stress ratio increases and decreases, respectively, with increasing strain. A slip event is most often due to the collapse of force chains by buckling and hence is accompanied by the release of stored energy, accumulated in force chains during the preceding stick event.

In what follows, we examine the evolution of the force

TABLE II: Summary of step numbers and strains for each group labeled data<sub>i</sub> in Figs. 21, 22.

Panel	data <sub>i</sub>	steps	$\epsilon$	
a	1	2-11	0.0067	0.0367
	2	12-21	0.04	0.07
	3	22-31	0.0733	0.1033
	4	32-41	0.1067	0.1367
	5	42-51	0.14	0.17
	6	52-63	0.1733	0.21
	7	64-73	0.2133	0.2433
	8	74-83	0.2467	0.2767
	9	84-86	0.28	0.2867
b	9	88-97	0.28	0.25
	8	98-107	0.2467	0.2167
	7	108-117	0.2133	0.1833
	6	118-127	0.18	0.15
	5	128-137	0.1467	0.1167
	4	138-147	0.1133	0.0833
	3	148-157	0.08	0.05
	2	158-167	0.0467	0.0167
	1	168-177	0.0133	-0.0167
c	1	178-187	-0.02	-0.05
	2	188-197	-0.0533	-0.0833
	3	198-207	-0.0867	-0.1167
	4	208-217	-0.12	-0.15
d	5	218-227	-0.1467	-0.1167
	4	228-237	-0.1133	-0.0833
	3	238-247	-0.08	-0.05
	2	248-257	-0.0467	-0.0167
	1	258-302	-0.0133	0

network and its effect on the macroscopic stress. We confine our attention to the different time steps for the forward shear. These data are from a run with a slightly higher density,  $\phi = 0.76$ . As shown earlier, the force network evolution in the forward and reverse shear cycles exhibit fairly universal statistics. To proceed, we employ two algorithms. The first identifies force chain particles via a so-called particle load vector. For each particle, the local force moment tensor,  $\hat{\sigma}_{ij}$ , as defined earlier, is computed. The largest eigenvalue of this tensor and its associated eigenvector are then used to define, respectively, the magnitude and direction of the particle load vector. The direction of force transmission is dictated by the direction of the particle load vector. Groups of particles whose particle load vectors line up within a predefined narrow angular range, and whose particle load magnitude is above the global average value, constitute a force chain. This procedure has been incorporated into an algorithm that takes contact force data as the known input, and provides the force chain particles, and hence the force chain particle network, as the output. Complete details of this procedure and its associated algorithm are provided elsewhere [16, 17].

The second algorithm was developed for the purposes of identifying parts of the force chain particle network that have undergone buckling, i.e. *buckled force chain “BFC” segments* [12]. A strain interval of interest,  $[\epsilon^A; \epsilon^B]$  is chosen: for example, that which spans a drop in stress ratio or an “unjamming event”, or a single time step in a DEM simulation. A set of

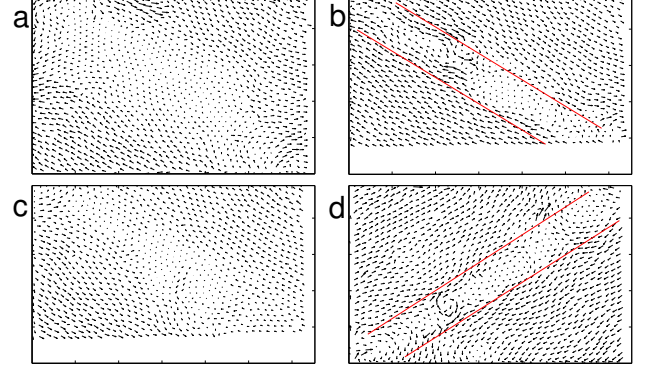


FIG. 23: Displacement fields showing shear bands in forward and reverse shear. These four fields correspond to the small particle displacement right after applying small deformations to the four images shown in Fig. 1. The red lines drawn in (b) (d) are a guide to the eye, indicating the regions of shear localization. Note that in parts (c) and (d) one or more side walls occupies part of the image.

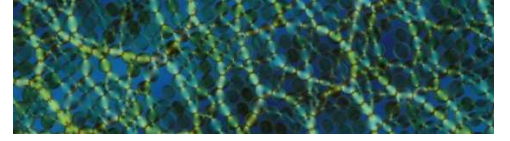


FIG. 24: Force chains in the shear band regime. This image is a slice of the main diagonal regime of image (b) in Fig. 1. Here the image is rotated to make the original diagonal line horizontal.

three filters is then applied: (a) eliminate all particles not in force chains at  $\epsilon^A$ ; (b) out of those remaining, eliminate those which have not decreased in potential energy; (c) out of those remaining, identify and isolate all 3-particle segments which have buckled. To determine if a segment has buckled, we consider the angle between the branch vectors from the central particle to the two outer particles. The decrease in this angle over the interval in question is defined as being twice the buckling angle,  $\theta_b$ . Then, a buckling segment is simply one where  $\theta_b > 0$ . The set of particles remaining after all three filters have been applied is the set referred to hereafter as BFCs. Later, we consider populations of BFCs in distinct subsets, where each subset is distinguished by a predefined nonzero buckling threshold  $\theta_b$  that member BFCs must satisfy over the given strain interval. Complete details of this entire procedure and associated algorithm are provided elsewhere [12].

The specimen deforms in the presence of a shear band, as shown in Fig. 23. The band is backward inclined in the forward shear and forward inclined in the reverse shear. As the material is sheared in a given direction, two triangular blocks slide over the shear band in opposing directions, effectively leading to simple shear across the shear band [18].

Although the material is dilated in the shear band, the force chains pass right through these bands, without substantial



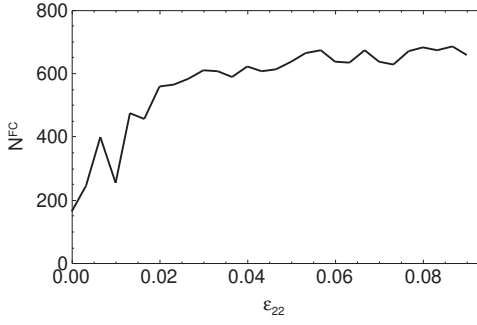


FIG. 25: Evolution with axial strain,  $\epsilon_{22}$ , of the population of force chain particles,  $N^{FC}$ .

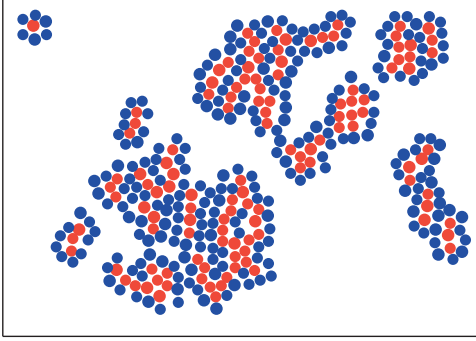


FIG. 26: Spatial distribution of force chain particles undergoing buckling (red) across the strain interval  $\epsilon_{22} = 0.060$  to  $0.077$ , together with their confining neighbors (blue). A buckling threshold of  $\theta_b = 2$  is used. Data shown here correspond to the central portion of the sample in the early stages of shear band development. We note that the width of the shear band narrows for higher strains.

changes, due to force balance (Fig. 24). During ‘stick events’, regimes of strain where the force network is stable, the primary force chains provide the major resistance to motion in the compressive direction. Weak secondary force chains still exist in the dilation direction and serve to ‘prop up’ the primary force chains. Primary force chains, laterally confined by weak network neighbors, are subject to axial compression and often fail via buckling. Secondary force chains, being in the direction of shear, tend to fail by extension.

As mentioned earlier (see discussion around Figs. 9 and 10), there is evidence of local failure events in the force network throughout the loading, both in the forward and reverse shear. These failure events are due to the continual collapse of old and formation of new force chains. The failures are concentrated mainly in the shear band where the mode of deformation of the material is essentially one of simple shear [18]. To unravel the mechanisms behind the hysteresis in the normal and shear components of stress, we examine the contribution to these stresses from force chains versus weak network particles. Recall that we confine our attention to the forward shear in the first shear cycle. In Fig. 25, we show the strain evolution of the population of force chain particles. As expected, there is an initial increase in the population as load is

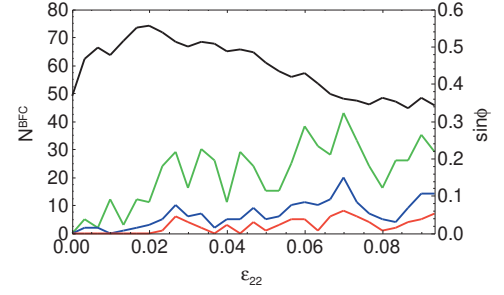


FIG. 27: Evolution with axial strain,  $\epsilon_{22}$ , of population of buckled force chain segments,  $N^{BFC}$ , for various buckling thresholds,  $\theta_b$ . Green, blue and red lines correspond to  $\theta_b = 1, 2$  and  $3$ , respectively. Also shown is stress ratio (black).

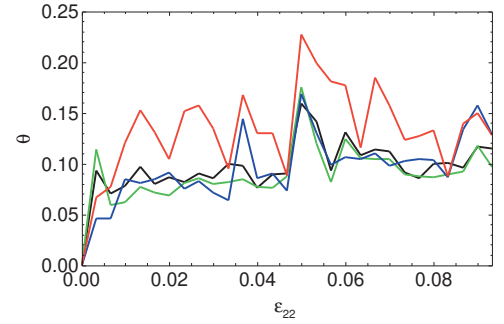


FIG. 28: Evolution with axial strain,  $\epsilon_{22}$ , of the relative rotation at contacts per step,  $\theta$ , for various types of contacts. Black, green, blue and red correspond to FC (force chain) to FC, FC to WN (weak network), WN to WN and BFC (buckling force chain) to BFC contacts, respectively. The unit of  $\theta$  is radians.

increased, followed by a near constant value for large strains. Note here, that the threshold value for the particle load vector (i.e. the global average) of each particle classified as a force chain is increasing with strain.

In light of Figs. 23b and 23d, the relative rotations between force chains are particularly relevant here. Discrete element simulations and photoelastic disk experiments of Oda and co-workers (e.g. [19, 20, 21, 22]) and by Veje et al. and Utter et al. [8, 9] have shown that particle rotations concentrate in the shear band. More recent studies confirm this, but additionally found that rotational motions dominate during slip events inside the shear band ([1, 12, 13]). These slip events are governed by the failure of force chains by buckling. The location and deformation periods during which relatively large particle rotations occur do indeed coincide with the location and incidences of force chain buckling: see Fig. 26 and Fig. 27. Rotation is a key mechanism in force chain buckling as is evident in Fig. 28 which shows that the greatest relative rotations are sustained at contacts between particles in buckling force chains.

## CONCLUSIONS

In this work, we have explored the evolution of force and contact networks for cyclic shear of a dense granular material. Starting from an initially unjammed low-density state, jamming occurs for sufficiently large shear. This is, in fact, associated with the phenomena of Reynolds dilatancy. In particular, during the first shear cycle, the system reaches  $Z = 3$  around step 70 corresponding to a shear strain of  $\epsilon = 23.3\%$ . During much of each cycle, the system is above a jamming threshold for which the mean contact number is  $Z' \approx 3$ . Although the stress components,  $Z$ , etc. are strongly hysteretic in strain, we empirically find that  $P$  is strongly correlated with the mean contact number when the system is jammed. The same is true for  $\tau$  vs.  $Z$  except immediately after a strain reversal, when  $\tau$  can become small. Again, excluding regions immediately following reversals, the mean values for  $P$  ( $Z$ ) and  $\tau$  approach zero linearly, within our resolution, as  $Z \rightarrow 3$  from above. In this case, the ratio  $\tau/P$  is, on average, constant.

We have applied a correction to the data to account for contacts which are below the experimental detection threshold. This correction was most important for very low stress states. For  $Z$ , the correction could reach  $\sim 15\%$ , although it was also applied to the pressure and the shear stress,  $\tau$ . The correction was implemented by assuming that the force distributions have (close to) universal exponential forms. A more accurate correction technique will be implemented in future work, but the present approximation is reasonable, given the statistical scatter of the data. We note that the jammed states are generally inhomogeneous in the density/packing fraction, since these are characterized by shear bands where the material is locally dilated and where much of the motion occurs.

We then analyzed the evolving force network in the forward shear using algorithms that distinguish contributions to macroscopic stress of particles from the strong and weak contact force network. Relatively large rotations develop during the buckling of force chains. These buckling events, which are present throughout the loading history, are primarily confined to the shear band and dominate during slip events or periods where stress ratio decreases with increasing strain. A detailed analysis of such internal failure events by buckling and their connection to structural evolution of the force and contact networks in cyclic shear loading is the subject of an

ongoing investigation.

**Acknowledgments** RPB acknowledges support from ARO grant W911NF-07-1-0131 and NSF grant DMR-0555431; AT acknowledges the support of the Australian Research Council (DP0772409) and the US Army Research Office (W911NF-07-1-0370).

- 
- [1] A. Tordesillas, J. Zhang, and R. P. Behringer, Geomechanics and Geoengineering (in press).
  - [2] T. Majmudar, M. Sperl, S. Luding, and R. Behringer, Phys. Rev. Lett. **98**, 058001 (2007).
  - [3] P. Dantu, Proc. Of the 4th International Conf. On Soil Mech. and Foundation Eng. **1**, 144 (1957).
  - [4] A. Drescher and G. de Josselin de Jong, J. Mech. Phys. Solids **20**, 337 (1972).
  - [5] T. Majmudar and R. Behringer, Nature **435**, 1079 (2005).
  - [6] T. Majmudar, PhD thesis, Duke University (2006).
  - [7] D. W. Howell, R. Behringer, and C. Veje, Phys. Rev. Lett. **82**, 5241 (1999).
  - [8] C. Veje, D. W. Howell, and R. Behringer, Phys. Rev. E **59**, 739 (1999).
  - [9] B. Utter and R. Behringer, Eur. Phys. J. E **14**, 373 (2004).
  - [10] B. Utter and R. Behringer, Phys. Rev. E **69**, 031308 (2004).
  - [11] B. Utter and R. Behringer, Phys. Rev. Lett. **100**, 208302 (2008).
  - [12] A. Tordesillas, Philosophical Magazine **87**, 4987 (2007).
  - [13] A. Tordesillas and M. Muthuswamy, Acta Geotechnica **3**, 225 (2008).
  - [14] B. Miller, C. O'Hern, and R. Behringer, Phys. Rev. Lett. **77**, 3110 (1996).
  - [15] F. Alonso-Marroquin, I. Vardoulakis, H. J. Herrmann, D. Weatherley, and P. Mora, Physical Review E **74**, 031306 (2006).
  - [16] M. Muthuswamy and A. Tordesillas, Journal of Statistical Mechanics - Theory and Experiment p. P09003 (2006).
  - [17] J. F. Peters, M. Muthuswamy, J. Wibowo, and A. Tordesillas, Physical Review E **72**, 041307 (2005).
  - [18] C. Thornton and L. Zhang, Philosophical Magazine **86**, 3425 (2006).
  - [19] M. Oda, J. Konishi, and S. Nemat-Nasser, Geotechnique **30**, 479 (1980).
  - [20] M. Oda and H. Kazama, Geotechnique **48**, 465 (1998).
  - [21] K. Iwashita and M. Oda, Powder Technology **109**, 192 (2000).
  - [22] M. Oda, T. Takemura, and M. Takahashi, Geotechnique **54**, 539 (2004).